Geomechanics for Energy and the Environment 35 (2023) 100488

Contents lists available at ScienceDirect

Geomechanics for Energy and the Environment

journal homepage: www.elsevier.com/locate/gete

The physics of desiccation cracks 1: Ductile fracturing and dependence on relative humidity

Ruoyu Chen *, Winston Lindqwister, Fei Wu, Boleslaw Mielniczuk, Tomasz Hueckel, Manolis Veveakis

Civil and Environmental Engineering, Duke University, Durham, 27708, NC, USA

ARTICLE INFO

Article history:
Received 15 May 2023
Accepted 11 July 2023
Available online 17 July 2023

Editors-in-Chief:
Professor Lyesse Laloui and Professor Tomasz Hueckel

Keywords:
Plascity
Desiccation crack
Triaxial test

ABSTRACT

Ductile deformation is ubiquitously found in the shrinkage of geomaterials. The existence of ductility requires elastoplastic mechanics when analyzing the structure deformation under external stress. In this work, we explore the physics of ductile fracturing based on the results from desiccation experiments and triaxial tests. By using the digital image correlation (DIC) method to generate the strain maps of samples undergoing desiccation cracking under different relative humidities, we obtain results showing the previously postulated Cnoidal Wave ductile failure patterns propagating under atmospheric condition-controlled crack velocities. We then correlate these observations with rate-dependent plasticity models calibrated through triaxial tests undergoing several unloading–reloading cycles and velocity stepping. This work demonstrates the necessity to consider ductility in soil cracking, indicating that the formation of crack patterns in soil desiccation is a slow and predictable process.

1. Introduction

Desiccation is a dehydration process found in almost every geomaterial, which causes volume shrinkage and may trigger disasters such as nuclear waste leakage and dam failure.[1,2] Structure failure in geomaterials resulting from desiccation is a complex phenomenon influenced by not only the material properties, including mineralogy and porosity but the external conditions, for instance, relative humidity and temperature.[3–8]

Different theoretical models have been proposed to describe soil failures, in which the most pertinent of those deriving from the theory of linear elastic fracture model (LEFM).[9–11] Hallett pointed out that LEFM can predict the deformation and strength in the ideal brittle and linear elastic soil.[12] And the widely accepted type of stress-controlled failure in LEFM for the desiccation crack is the tensile failure, in which cracks appear when the effective tensile stress exceeds the tensile strength,[13] which is not randomly distributed but follows a specific pattern.[14]

Despite the widely accepted nature of LEFM, when it is applied to the problem of soil desiccation, LEFM has several shortcomings. These include lacking the information to predict the crack patterns, predicting a crack propagation velocity of the order of the speed of elastic sound, and assuming that the soil material is linear elastic until failure. The latter has been pointed out repeatedly since the plasticity of the wet soil is essential and must be included in the deformation mechanisms.[15–17]

In this work, we treat the crack as ductile instead of brittle considering the plastic deformation found in soil.[11,18] The ductility in the geomaterials is revealed based on desiccation experiments at controlled humidities and triaxial tests. The pattern of cracks in the desiccation process is discussed following the rate-dependent viscoplastic mathematical model developed recently by Refs. 19, 20. The crack propagation velocity under different relative humidity is posted and juxtaposed to the fracture mechanics predictions. We show that the introduction of viscoplastic (ductile) considerations stemming from the evaporation and shrinkage rates can predict the pattern of cracks as the singularities solutions from the Cnoidal wave equation developed by Refs. 19, 20.

We are validating our assumptions through digital image correlation (DIC) analysis to obtain a continuous strain field with the surface images, by which the strain field and the propagation velocity of cracks can be recorded and visualized without soil disruption.[21,22] The reversible deformation follows the linear elastic relation with soil Young's modulus.[23] For the plastic portion, a standard power law including the strain rate and effective stress to describe the plastic deformation considering dilatancy property in the soil.[19,24,25] The value of the power, known as rate sensitivity, is influenced by the physical properties of geomaterials.[25] With the strain maps and the strain–stress relation, the stress can be calculated and used to predict ductile soil failure and fracturing.

* Corresponding author.
E-mail address: ruoyu.chen@duke.edu (R. Chen).

https://doi.org/10.1016/j.gete.2023.100488
2352-3808/

Table 1
Physical properties of the geomaterial.

Characteristics	Specific gravity	Liquid limit	Plastic limit	Young's modulus	Shear modulus	Poisson's ratio
Values	2.892	25.02%	17.15%	8.6 Mpa	3.3 Mpa	0.2857

Young's modulus, shear modulus, and Poisson's ratio are calculated from fully-saturated geomaterial.

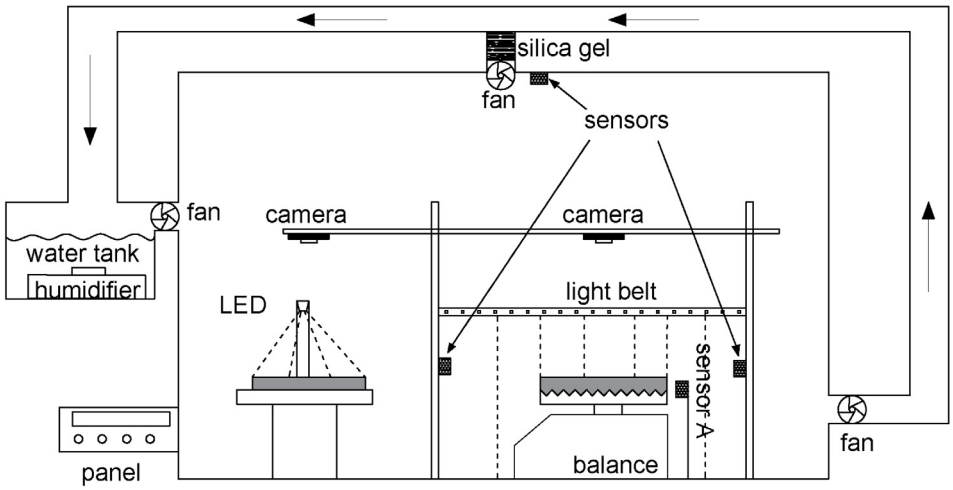

Fig. 1. The atmospheric chamber with humidity controllers. The left sample lies on the PTFE plate; the right sample lies on the platform with constraints; the panel controls and monitors the humidity based on three sensors; the sensor next to the sample, sensor A, records atmospheric conditions and sends them to the connected laptop.

2. Materials and methods

In this work, we have performed two types of experiments on the same material: desiccation tests in an atmospheric chamber and triaxial tests. This section details both approaches. In both campaigns, we have used granite powder with an average grain size of the order of 50 μm, mixed with distilled water to create a silt. The properties of the silt used in the tests are shown in Table 1. The specific gravity, liquid limit, and plastic limit were measured following the classical soil mechanics tests.[26] Young's modulus, shear modulus, and Poisson's ratio were calculated based on the volumetric strain and pressure in consolidation tests.[27]

2.1. Desiccation tests in atmospheric chamber

Desiccation tests were conducted in an atmospheric conditions-controlled chamber shown in Fig. 1. The geomaterial powder was mixed with distilled water and shaped into rectangles with the help of a mold whose inner dimension is 150 mm (length) × 50 mm (width) × 14 mm (height). The initial gravity water content is 33 ± 3%. There are two samples in one test, one on a polytetrafluoroethylene (PTFE) platform as the reference group and the other on a 3D-printed 90-degree constraint platform. The temperature in these tests was set to room temperature, 25 ± 1 °C. The relative humidity (RH) was controlled under the combined effect of silica gel and a water humidifier. Data, including temperature and relative humidity, were measured and transited to the desktop every 6 s by Sensor A. Two Canon EOS 4000D were used to capture the surface images every 60 s.

The top surface image series captured by the cameras were processed by the DIC software developed by Blaber.[28] Due to the capacity of the desktop, the image series starts several minutes before the crack onsets to the moment that cracks are fully developed cracks. We used XnView software to rotate and crop the original images to obtain a rectangle region in which the sample's edges are parallel to the edges of the image. The first image in the series was selected as the reference image, and the other images were the 'current' images at different times.

The sample's surface in the processed images was selected as the region of interest (ROI), divided into circular groups containing several pixels called 'subsets'. Based on the normalized cross-correlation and the inverse compositional Gauss–Newton method as the non-linear optimization scheme, the DIC algorithms correlate the subsets in 'current' images with the subsets in the reference image and calculate the deformation.[28,29]

The Green–Lagrangian strains of the surface were calculated from the subsets displacement following the DIC analysis described in Ref. 30. In these strain tensors, the negative value represents compression, and the positive value means tension. The results from the desiccation test with DIC analysis include the pattern of cracks, the strain map on the sample surface, and the crack propagation velocity on the macro-scale.

2.2. Triaxial experiment

The triaxial test shows the property of elastoplasticity and rate sensitivity in the process of soil deformation. 3D-printed polylactic acid (PLA) tubes, whose height and inner diameter are 80 mm and 35 mm, were selected to remold the samples. The sample used in the triaxial test was prepared following the same preparation step in the desiccation test, and the sample was transferred into the PLA tubes on a disposal pan with a spatula. After placing the mixture in the PLA tube, we used a soil pestle to compact the mixture for a flat surface and a relatively homogeneous porosity. The tube and pan were left undistributed till the total mass stopped decreasing, generally one week. Then, the tube and pan were removed, and the cylindrical sample was ready for the triaxial test shown in Fig. 2(a).

The water content and porosity of the samples are sought because the rate sensitivity and void ratio are highly related to them. Based on the initial water content and mass measured by the precise laboratory moisture analyzer, RAD WAG MA 50/1.R.,

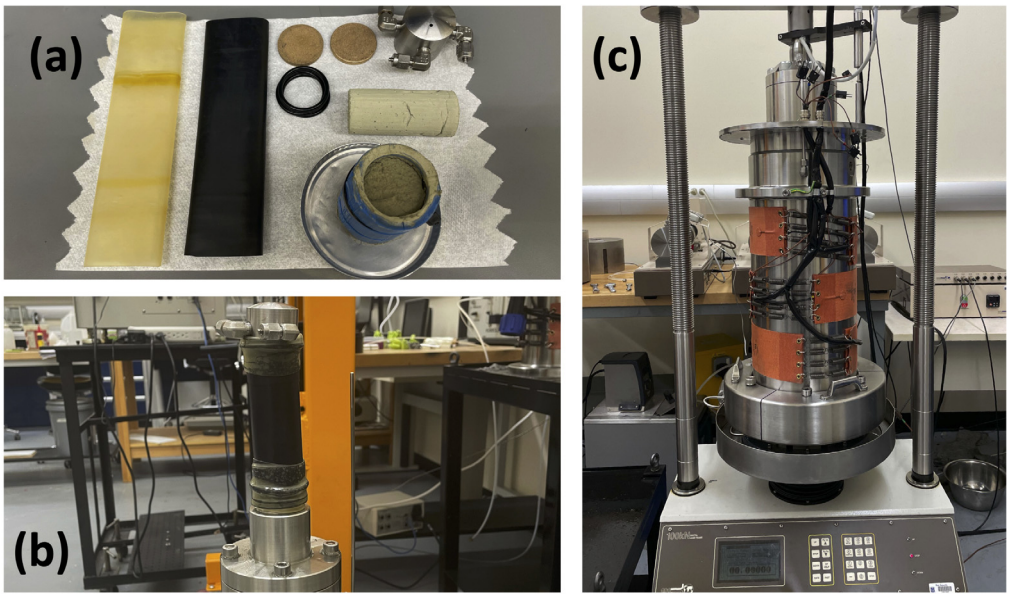

Fig. 2. Sample preparation and the triaxial machine. (a) two kinds of membranes, the porous stones, o-rings, cap, prepared sample, and sample with PLA tube and disposal pan; (b) the sample covered with membranes stands on the base; (c) the assembled triaxial cell on the loading frame.

and laboratory balance, Adventurer Pro AV812C, with a readability of 0.01 g, the water content (ω) and porosity (ϕ) were calculated following the formula:

$$\omega = \frac{m_3 - (m_2 - m_1)(1 - \omega_i)}{(m_2 - m_1)(1 - \omega_i)} \tag{1}$$

$$\phi = \frac{V_t - V_s - V_w}{V_t} \tag{2}$$

$$V_t = \frac{\pi h d^2}{4} \tag{3}$$

$$V_s = \frac{(m_2 - m_1)(1 - \omega_i)}{\rho_s} \tag{4}$$

$$V_w = \frac{m_3 - (m_2 - m_1)(1 - \omega_i)}{\rho_w} \tag{5}$$

where

$m_1 = mass\ of\ the\ tube + mass\ of\ the\ disposal\ pan$

$m_2 = mass\ of\ the\ tube + mass\ of\ the\ disposal\ pan + mass\ of\ wet\ sample$

$m_3 = mass\ of\ dried\ sample$

$\omega_i = initial\ water\ content$

$h = height\ of\ the\ sample$

$d = diameter\ of\ the\ sample$

$\rho_s = specific\ density\ of\ the\ soil$

$\rho_w = water\ density$

The fluid used in the triaxial machine to maintain the confining pressure is silicone-based bath fluid, JULABO Thermal H10. The sample was sealed by a Latex membrane and a silicon butyl rubber membrane. Two porous stones were put at the top and bottom of the sample inside the membranes, and the cap was installed on the top of the sample. Shown in Fig. 2(b), four o-rings, two at the top and two at the bottom, were used to seal the membranes. After the setup of the sample on the platform, the outer tank was moved to the platform and assembled together. Then the main body was transported to the loading frame for the triaxial test shown in Fig. 2(c).

The triaxial test was divided into different stages controlled by the desktop connected to the triaxial machine. The loading and unloading processes are controlled by positive and negative axial displacement velocity, which can be interpreted as controlled axial strain rate ($\dot{\epsilon}_{axial} = v_i/h$) processes. In the first stage, the confining pressure, which is the radial stress, increased to the desired value and stayed constant till the end of the test. In the next stage, the loading frame lifts the sample at a constant velocity, v_{ref}. Then the sample went through three unloading–loading cycles. After these cycles, the loading process continues to the ultimate stress stage. When the deviatoric stress reaches the ultimate value, different loading velocities (v_i) are applied to the samples. The loading velocity was again set to v_{ref} in the final stage.

3. Results

3.1. Morphology

In the desiccation process, the samples experienced different shrinkage stages, including normal, residual, and no shrinkage stages. The cracks appeared only on the constraint platform experiment in the normal shrinkage stage, while no cracks were observed on the PTFE platform. In the constraint experiment where the constraint direction is parallel to the y-direction, the sample can freely shrink in the y-direction but has resistance from basal constraint along the x-direction. The cropped surface images, which are sprayed with black paint to increase the contrast for the accuracy in DIC analysis, are shown as (a1),(b1), and (c1) in Fig. 3, where the white line represents the middle line of the sample.

The image series (a2), (b2), and (c2) shows the magnitude development of ϵ_{xx} and ϵ_{yy} along the middle line. (a2) indicates a smooth flat curve representing the normal shrinkage in both x- and y-direction on the surface before the appearance of cracks. The sign of ϵ_{xx} and ϵ_{yy} are opposite at the location of prospective crack with a magnitude of 10^{-4} as shown in the zoom-in figure in (a2). At the initiation of the first failure, the positive peak of ϵ_{xx} is surrounded by two symmetry negative concaves shown in (b2), while the ϵ_{yy} distribution is still flat. In the following stage, the second crack appeared and developed, and the two positive ϵ_{xx} peaks in (c2) represented the locations of two cracks along the middle line. Negative ϵ_{xx} regions are found near the cracks, and

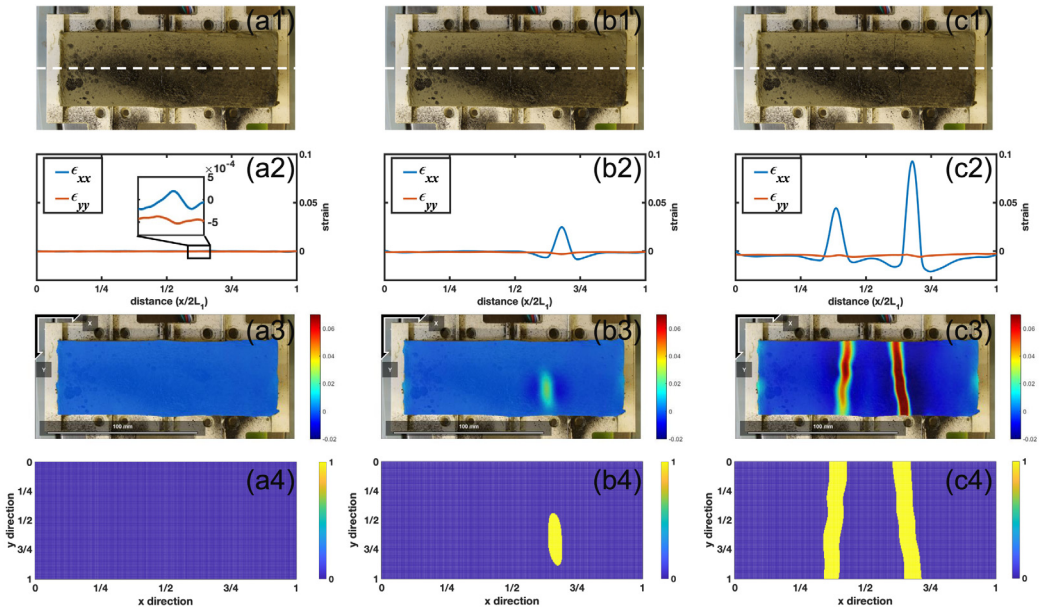

Fig. 3. Surface images of 90-degree constraints test with 76% humidity. The reference image was captured at 1212 min, the current image in group (a) was taken 10 min after the reference image, the current image in group (b) was taken 35 min after the reference image, the current image in group (c) was taken 150 min after the reference image. (a1), (b1), and (c1) are the cropped images captured by the camera; (a2), (b2), and (c2) are ϵ_{xx} and ϵ_{yy} distribution along the middle line where $2L_1$ representing the total length of the sample; (a3), (b3), and (c3) are ϵ_{xx} maps on the top surface processed by DIC method; (a4), (b4), and (c4) are the bifurcation images of crack existence with the threshold (0.009).

ϵ_{yy} stays stationary along the middle line. The strain distribution shows that $\epsilon_{xx} \gg \epsilon_{yy}$, and the magnitude difference between the strains permits to use of ϵ_{xx} to determine the failures in the samples.

(a3), (b3), and (c3) give the ϵ_{xx} on the top surface generated by DIC method. The crack region in (b3) shows the negative strain regions only exist at the left and right sides of the cracks. The upper and lower regions have positive strains with smaller values, shown as lighter color parts in the image, indicating that the crack propagates in the *y*-direction. (c3) gives the strain map with two fully developed cracks propagating throughout the sample, and some positive regions at the sample's left and right sides represent the curling of the edges.[31]

The bifurcation maps are used to identify the existence of cracks. The blue segments are '0', representing the continuous plain surface, and the yellow segments are '1', representing the areas of cracks. No failure region is found in (a4). One crack is found as the yellow region in (b4). And two fully developed cracks are shown in (c4). The ϵ_{xx} strain threshold for the bifurcation is 0.009.

3.2. Crack propagation

The bifurcation maps provide visual failure regions. These regions' maximum length and width are treated as the length and width of cracks. The length is defined as the distance in the *y*-direction, while the width is the distance in the *x*-direction. Despite not capturing the dynamics of crack tip propagation because of the 1 min interval of images, the development of failure region still provides a comprehensive understanding of the ductility in the desiccation cracks due to the slow timescale of propagation of the crack.

The desiccation cracks show up when the water content decreases to a critical value.[13] As the evaporation rate has a negative linear relationship with the relative humidity in the first evaporation stage,[27] the cracks appeared later with higher humidity than in the lower humidity experiment because more time is needed for sample in higher humidity to reach the critical water content.

The first crack appears at 565 min, and the second at 586 min when the relative humidity is 35%. This sample has developed along the *y*-direction as the length reached 49 mm. And the width of the first crack is 10.8 mm and 10.3 mm for the second crack, shown in Fig. 4(i). When the humidity is set to 45%, the onset of the first crack is 633 min, and the second crack is 683 min. In this test, the length of the fully developed cracks is 50 mm, and the width is 7.9 mm for both cracks. For a more moist experiment, where the relative humidity is 90%, the onset of the first crack is 1510 min, and the onset of the second crack is 1806 min. In this test, the length of the cracks is 50 mm, and the width is 8.4 mm for these two cracks. The length and width of cracks develop at a constant velocity, followed by a slow-down stage at the end due to the edge influence.

3.3. Triaxial tests

The triaxial experiment is the axial velocity-controlled consolidated undrained test. The height and diameter of the cylindrical sample used in Fig. 5 are 75.37 mm and 34.55 mm. The water content is 12%, and the porosity is 46.56%. The confining pressure in this test is set to 300 kpa. Three unloading–reloading cycles were conducted for the unloading–reloading modulus E_{ur} with $v_{ref} = 0.5$ mm/min. After the sample reached the ultimate deviatoric stress, the loading velocity was changed into different values and set back to 0.5 mm/min in the final stage.

The corresponding unloading–reloading modulus is 2.21 Mpa, 2.87 Mpa, and 2.51 Mpa in the first, second, and third cycles. The zoom-in figure in Fig. 5 shows the ultimate deviatoric stress in different stages. The loading decreased from 0.50 mm/min to 0.05 mm/min by four steps and increased to 1.00 mm/min in five steps. In stage 1, the loading velocity is 0.50 mm/min referring to 0.663%/min as the axial strain rate, where the ultimate stress is 1290 kpa. In stage 2, the loading velocity is 0.25 mm/min referring to 0.331%/min as the axial strain rate, where the ultimate stress is 1280 kpa. In stage 3, the loading velocity is 0.10 mm/min referring to 0.133%/min as the axial strain rate, where the ultimate stress is 1262 kpa. In stage 4, the loading

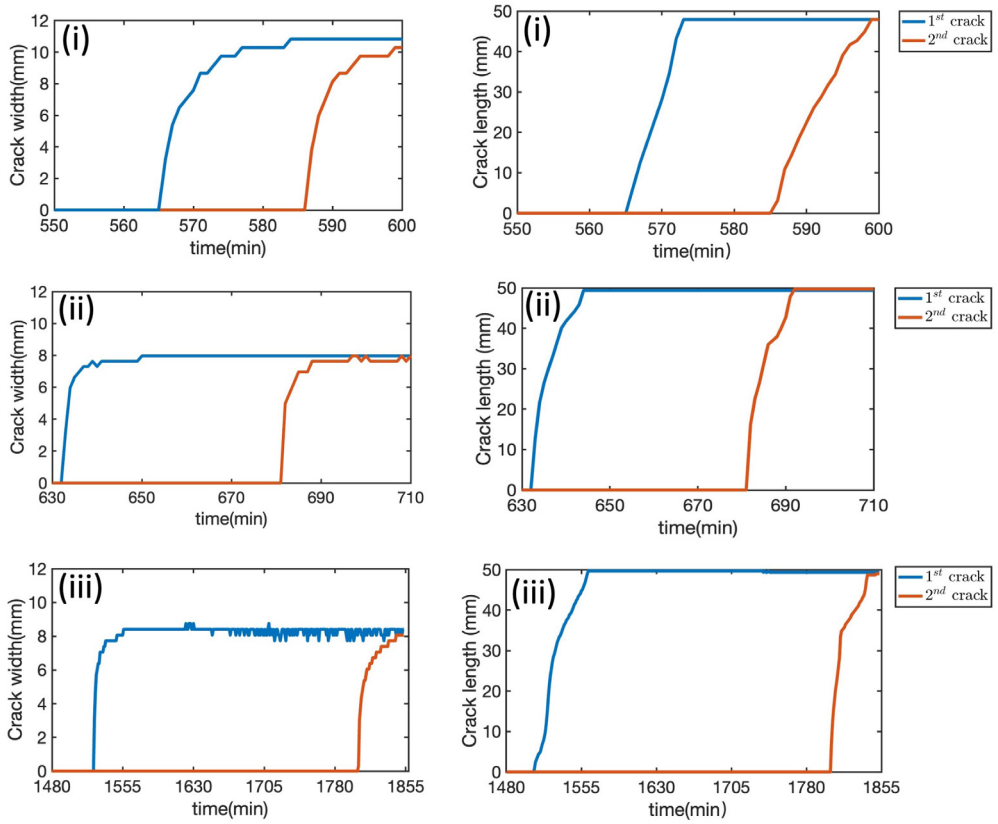

Fig. 4. Width and length development with different relative humidity.(i) are the results from 35% relative humidity, (ii) are the results from 45%, and (ii) are the results from 90%.

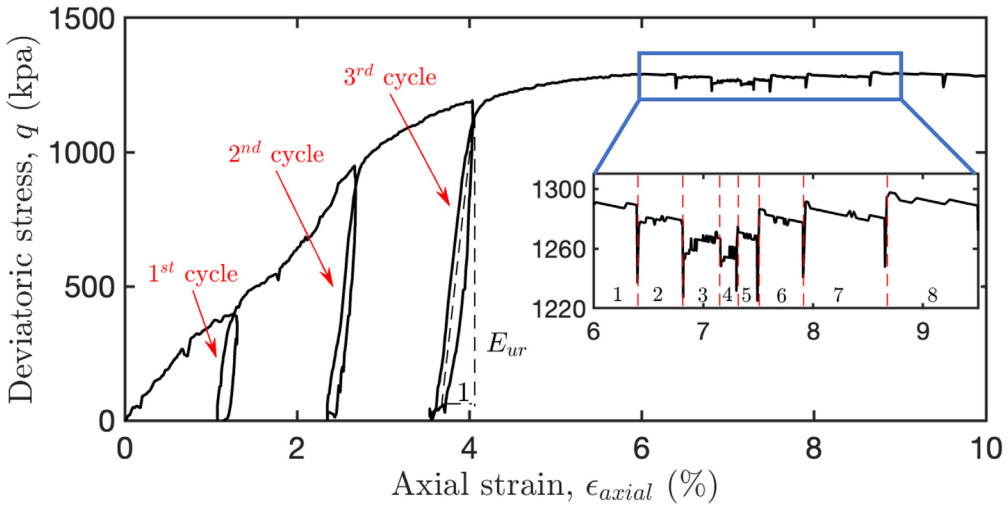

Fig. 5. Results from the triaxial experiment with three unloading–reloading cycles and different loading rates.

velocity is 0.05 mm/min referring to 0.066%/min as the axial strain rate, where the ultimate stress is 1253 kpa. In stage 5, the loading velocity is 0.10 mm/min referring to 0.133%/min as the axial strain rate, where the ultimate stress is 1266 kpa. In stage 6, the loading velocity is 0.25 mm/min referring to 0.331%/min as the axial strain rate, where the ultimate stress is 1280 kpa. In stage 7, the loading velocity is 0.50 mm/min referring to 0.663%/min as the axial strain rate, where the ultimate stress is 1282 kpa. In stage 8, the loading velocity is 1.00 mm/min referring to 1.33%/min as the axial strain rate, where the ultimate stress is 1293 kpa.

4. Discussion

The results from DIC and triaxial tests offer some insights into the geomaterials' ductility. This section will provide the pattern of cracks with viscoplasticity, a discussion on the propagation velocity, the elastoplastic deformation in the triaxial test, and the rate sensitivity.

4.1. The pattern of cracks

Our experiments were conducted on the constraints platform, providing shrinkage resistance from the bottom in the

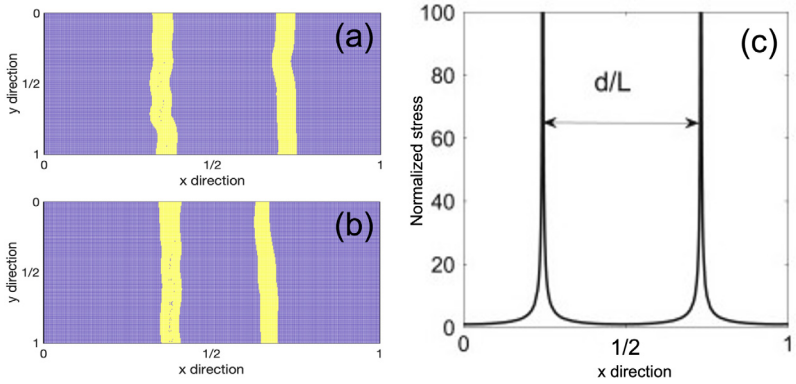

Fig. 6. Locations of cracks on the constraint experiments with different relative humidity, and the singularity solutions from Eq. (6). The relative humidity is 45% in (a) and 90% in (b). (c) is cited and adjusted from Ref. 20, which shows the numerical stress distribution in the x-direction for $m = 3$ and $\lambda = 60$.

x-direction. The resistance generated extra stress along the x-direction, contributing to the increment of total stress. The magnitude difference of strain in the x and y-direction shown in Fig. 3 allows treating the sample as an idealized one-dimension tension model along the x-direction.

The stress peaks in the simplified model distribute following the solutions from the Cnoidal wave equation, which is a periodic pattern. Veveakis proposed the mathematical model of the Cnoidal wave equation in the viscoplastic geomaterial,[32] and the simplified 1D equation is shown as:

$$\frac{\partial^2 \sigma'_{xx}}{\partial x^2} - \lambda {\sigma'_{xx}}^m = 0 \tag{6}$$

where σ'_{xx} is the nondimensional effective stress along the x-direction, $x = X/2L_1$ is the normalized distance in the x-direction, λ is a dimensionless parameter from the combination of the sample's physical characteristics and loading velocity, and m is the rate sensitivity that is larger than 1 for geomaterials. For the periodical model, the wavelength and number of peaks, referring to the distance between cracks and the number of cracks, are determined by a combination of λ and m. The analytical ($3 > m > 1$) and numerical ($m \geq 3$) solutions of the equation with different m are calculated (one example is shown in Fig. 6(c)), which symmetrically distribute along the x-direction.[19]

Experiments with different relative humidity were conducted, and different relative humidities give different shrinkage rates, which change the λ. All the cracks in the experiments were found parallel to the constraint direction and distributed at the locations of stress peaks in Eq. (6). The cracks divided the rectangle samples into three parts, and the left and right parts are symmetrical, with the spacing influenced by relative humidity instead of randomly distributed, as shown in Fig. 6(a) and (b).

Though only two cracks were observed in our experiment, the morphology of cracks from other researchers provides the pattern where more cracks are found in the rectangle sample shown in Fig. 7.[33] The difference in geomaterial characteristics and sample dimension causes the difference in crack number in the 1D constraint experiments. Still, the location of cracks distributed following the Cnoidal wave format is consistent in all the experiments.

The extension of 1D equation to 2D equation is given by Ref. 32 as the following formulation:

$$\frac{\partial^2 \sigma'}{\partial x^2} + \frac{\partial^2 \sigma'}{\partial y^2} - \lambda {\sigma'}^m = 0 \tag{7}$$

with the assumption that the sample is homogeneous, symmetrical, and under isotropic extension in x- and y-directions. The numerical finite element solutions of the equation suggest that the location of stress singularities appears in a periodic pattern in both directions. And the singularities split the sample into symmetrical sub-regions with the shape of polygons, including triangles, squares, and hexagons.[32,34] Angles of the intersection for these shapes are 90° and 120°

Based on the test produced by Peron shown as the right image in Fig. 7, the cracks in the 2D constraint square have three or four intersections except for the boundary.[33] The range of angles is 90° to 150°, with the angle of circled intersections is 120°. Regions formed by these cracks are polygons, from triangles to hexagons. The bias between the mathematical model and experimental results may come from the influence of discontinuity. After the formation of the primary cracks, the error exists when using continuous equations to describe the discontinuous sample. Though the porosity singularities have the same location as stress singularities, which allows treating samples with cracks as continuous, the stress relief and energy dissipation need to be included in the prediction of secondary cracks.[20,35] The superimposed stress from the viscoplasticity model and stress relief gives the pattern of the secondary cracks and is responsible for the deviation between the shape of secondary cracks with the predicted polygons.

The other point is that the stress wave inside the sample has preferred peak locations. In idealized purely brittle materials, the stress could fully transmit in the material.[36] In this circumstance, the crack should randomly distribute on the surface without any patterns as no preferred stress peak locations exist, which contrasts with the experimental results. The explanation for contrast is the existence of viscoplasticity in the geomaterial, with which proposed the stress wave can only partially transmit in the material.[36] And the portion of stress transmission can be conceptualized as the ratio between external deformation and inner melt phase movement. The superposition of stress in elastic and viscoplastic waves leads to the stress peaks on the samples, which are shown as parallel cracks following the Cnoidal wave in the 1D constraint experiment and the polygons regions in the 2D constraint experiment.

4.2. Crack propagation velocity

The evaporation causes volume shrinkage and water content decrement, generating resistance from basal constraint and suction increment. The superposed stress leads to the initiation of cracks once exceeding the tensile strength. Once cracks appear, the crack tips develop along the y-direction till reaching the edges of the sample, contributing to the length change. The average velocity, which is the total length of the crack divided by the time of the propagation period, is underlined in this section.

The ductility of desiccation cracks first appears in the rate-dependent characteristic of the geomaterial. The atmospheric

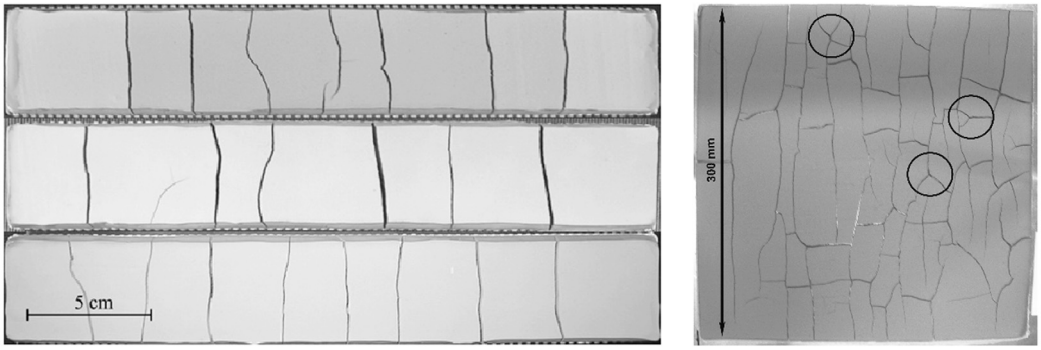

Fig. 7. The morphology of cracks produced by Peron.[33] The left image is the result of the one-dimensional constraint experiments. The right image is from the two-dimensional constraint experiment.

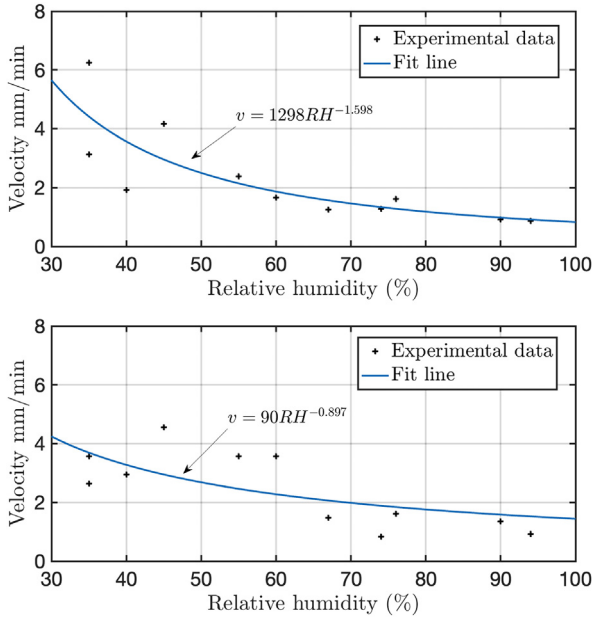

Fig. 8. Length propagation velocity in different relative humidity. The upper image is the average velocity of the first cracks; The lower image is the average velocity of the second cracks.

conditions, which is the relative humidity in this work, changed the volumetric strain rate. The negative linear relationship between the relative humidity and volumetric strain rate in the constant rate evaporation stage.[27] At the same time, crack length propagation velocities exhibited a negative power relation with relative humidities shown as the fit lines in Fig. 8 in both the first and second cracks. This rate-dependent propagation also provides the necessity to include the ductility of the geomaterial when analyzing the mechanics.

Another appearance of ductility is the magnitude of velocity. All propagation velocities locate in the same magnitude instead of being the rapid opening found in the brittle materials, which is 200 m/s−350 m/s.[37] The first cracks develop faster than the second groups in three groups when relative humidities are 35%, 35%, and 74%. The maximum difference is 2.68 mm/min in the experiment with 35% humidity. When the relative humidity is 76%, the propagation velocities are exactly the same for the first and second cracks. For the other experiment with 40%, 45%, 55%, 60%, 67%, 90%, and 94% humidity, the second cracks develop faster than the first cracks, with the maximum difference being 1.90 mm/min in the 60% test. The velocity competition between the first and second cracks does not show a clear preference in the experiments conducted in this research. Besides, the results in Fig. 4 contain a linear portion during the initial portion of crack development, but the propagation slows down when the cracks are about to reach the edges. This means the length of cracks does not change the velocity, while the boundaries of samples have a significant influence.

The development of crack tips is discussed through fracture mechanics to interpret the power law relationship between propagation velocity and relative humidity. Desiccation cracks obtained from experiments are designated as Mode I failures. The crack tips velocity is described as[38]:

$$v = A\left(\frac{K_I}{K_{Ic}}\right)^n \tag{8}$$

in which v is crack tip velocity, K_I is the stress intensity factor, K_{Ic} is plane strain fracture toughness, A and n are material coefficients. The variable that changes in different groups is K_I. In our desiccation experiment, which can be simplified as a finite plate with uniform uniaxial stress that comes from evaporation, the adjusted K_I is[39]:

$$K_I = \sigma'_{xx} \cdot \sqrt{\pi a} \cdot f\left(\frac{a}{w}\right) \tag{9}$$

where a is the length of crack, and w is the width of the sample. The velocities in Fig. 8 are calculated based on linear portions with the same crack length, same a. Meanwhile, the geomaterial and the sample dimension are the same in all the tests. The correlation between the only variable in different tests, σ'_{xx}, with volumetric strain rate is revealed with the help of the power law rheology[20,40]:

$$\sigma'_{xx} = B\dot{\epsilon_v}^{\frac{1}{m}} \tag{10}$$

where B is nondimensional reference stress, and $\dot{\epsilon_v}$ is the nondimensional volumetric strain rate, which is irreversible once the crack generates, that linearly relates to relative humidity. The influence of relative humidity on the propagation velocity is found by substituting Eqs. (10) and (9) into Eq. (8) as:

$$v = C_1\dot{\epsilon_v}^{\frac{n}{m}} = C_2 RH^{\frac{n}{m}} \tag{11}$$

in which C_1, C_2, and n are combinations of sample properties, including geomaterial characteristics and sample dimension, while m is the rate sensitivity. Eq. (8) explains the power law fit line shown in Fig. 8, also shows the velocity for the 1st and 2nd cracks should be the same in the test under the same relative humidity. The velocity deviation from experimental results may come from the stress relief once the 1st crack appears, causing the change of σ'_{xx}. The velocity difference between the 1st and 2nd cracks results from the variation of dimension, as the ratio between the width and length of samples changes.

Table 2
Reversible and irreversible strain in the unloading–reloading cycles.

Unloading–reloading cycle sequence	Reversible strain	Irreversible strain	Total strain	Portion of irreversible strain	Modulus	Axial loading velocity
1	0.18%	1.08%	1.26%	85.7%	2.21 Mpa	0.5 mm/min
2	0.29%	2.39%	2.68%	89.2%	2.87 Mpa	0.5 mm/min
3	0.42%	3.62%	4.04%	89.6%	2.51 Mpa	0.5 mm/min

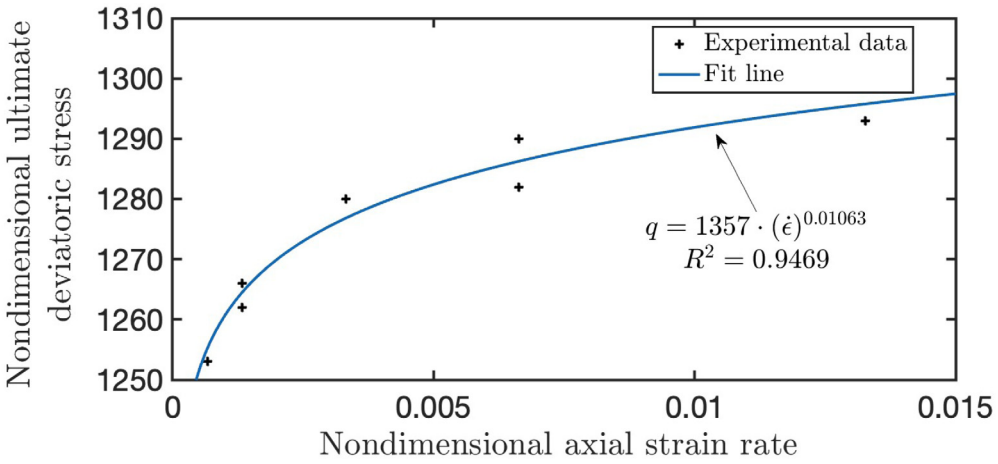

Fig. 9. The nondimensional ultimate deviatoric stress in the triaxial test with different non-dimensional axial loading rates.

4.3. Triaxial test

The deformation in the triaxial test is a combination of reversible and irreversible displacement, which requires elastic and viscoplastic analysis during the constant loading velocity stage.[41] This combination can be shown as:

$$\epsilon_v^t = \epsilon_v^r + \epsilon_v^{ir} \tag{12}$$

and the strain rate is:

$$\dot{\epsilon}_v^t = \dot{\epsilon}_v^r + \dot{\epsilon}_v^{ir} \tag{13}$$

where t, r, ir in the headers means total, reversible, and irreversible. Based on the results before the ultimate deviatoric stress shown in Fig. 5, Table 2 exhibits the value and portion of reversible and irreversible strain in three unloading–reloading cycles. The elastic part is the difference between strain at the unloading and reloading onsets in each cycle, while the leftover strain is irreversible. The unloading–reloading modulus, E_{ur}, has an average value of 2.53 Mpa in the process of the triaxial experiment before the stress reaches the ultimate value. Meanwhile, the portion of irreversible strain increases.

A linear relation between reversible strain and stress is applied with the unloading–reloading modulus. And the irreversible part, which is rate sensitive, is shown as the adjusted Eq. (10).[20,42] Then the strain-stress relation in the triaxial test has the following formulations:

$$\dot{\epsilon}_v^r = \frac{\dot{q}}{E_{ur}} \tag{14}$$

$$\dot{\epsilon}_v^{ir} = (\frac{q}{B})^m \tag{15}$$

$$\dot{\epsilon}_v^t = \frac{\dot{q}}{E_{ur}} + (\frac{q}{B})^m \tag{16}$$

where the strain rates and deviatoric stress are non-dimensional. As the loading velocity is constant before different velocities stages, the summation of reversible and irreversible strain rates is constant. So the stress acceleration becomes lower when stress becomes higher, as shown in Eq. (16). This relation also explains the increment portion of irreversible strain when the stress increases. The elastic reversible stain rate decreases when the stress acceleration becomes lower. Meanwhile, the irreversible plastic strain rate increases due to stress increases. And the strain softening was observed the ultimate stress was larger than the residual stress with the same loading velocity.[43,44] Due to the lack of microscale experiments on the geomaterial, our interest focuses on the different ultimate stress with various velocities instead of the softening process.

The ultimate stress in the stress–strain curve shown in Fig. 5 represents the point where the stress rate becomes zero. When $\dot{q}$ is zero, total strain change equals the irreversible strain, which provides a method to evaluate the rate sensitivity of the geomaterial by comparing the ultimate stress under different loading velocities. When loading velocity changes, lower stress was found at lower loading velocities.[45] The curve in Fig. 9 clearly shows the viscoplastic behavior in this sample with the rate sensitivity $m = 94.1$.

5. Conclusion

Desiccation cracks were shown in this contribution not to obey the properties expected by the theory of linear elastic fracture mechanics for brittle cracking. It was shown that the cracks are driven and propagate under the combined influence of evaporation and shrinkage rates of the soil. And the patterns forming are not random but predictably repeatable. All these results were discussed and revealed the need to account for rate-dependent in shrinking geomaterials. With the help of these experiments and analysis, the main conclusions are drawn as follows:

- 1D constraint experiments have cracks parallel to the constraint direction,[46] while polygons cracks are found in the 2D constraint experiment.[31] As the crack locations represent the stress peaks, the pattern of cracks in both 1D and 2D experiments indicates the stress peaks distribution, which is consistent with the singularities in the viscoplasticity model. Besides, instead of the random probability of generating failure on the surface in the purely elastic brittle material, the preferred pattern of failure requires researchers to treat geomaterials as ductile and consider the stress wave transfer in elastoplastic materials.

- Based on the DIC method, the crack propagation velocity in the 1D constraint experiment shows a relation with relative humidity which controls the volumetric strain rate. Instead of rapid fracture, the magnitude of crack propagation velocity is relatively small. The influence of humidity is interpreted through the fracture mechanics with the mode I fracture and the rate-dependent strain-stress relation from the viscoplasticity.
- The portion of irreversible deformation in the strain-controlled triaxial experiment increases during the loading process. The unloading–reloading modulus from three cycles stays at the constant value. At the constant strain rate, the irreversible strain rate increases due to the deviatoric stress increment. The reversible strain rate decreases as the deviatoric stress rate decreases. When the deviatoric stress reaches the ultimate value, the deviatoric stress rate becomes zero, and all the deformation is irreversible.
- The ultimate deviatoric stress increases when the axial strain rate increases following a power-law relationship. The rate sensitivity of the sample is 94.1, and the reference stress is 1357 Kpa. This rate-dependent relationship indicates the viscoplastic property of the sample, and provides evidence to include the ductility in the desiccation cracks.

Rate sensitivity, a significant parameter inside the geomaterials, is exhibited in this paper's triaxial and desiccation test as a sign of ductility in the geomaterials. Instead of analyzing soil desiccation in a linear elastic fracture mechanics way, elastoplasticity, including a linear elastic portion and another power-law plastic portion with rate sensitivity, needs to be adopted. Such an approach is presented in our companion paper.[47]

CRediT authorship contribution statement

Ruoyu Chen: Analysis, Writing – original draft, Data analyses. **Winston Lindqwister:** Software. **Fei Wu:** Methodology. **Boleslaw Mielniczuk:** Methodology. **Tomasz Hueckel:** Supervision, Funding acquisition. **Manolis Veveakis:** Supervision, Conception of the study, Funding acquisition.

Declaration of competing interest

The authors declare that they have no known competing financial interests or personal relationships that could have appeared to influence the work reported in this paper.

Data availability

Data will be made available on request.

Acknowledgments

The authors gratefully acknowledge the support of the U.S. Department of Energy grant DE-NE0008746 and the U.S. National Science Foundation for project CMMI-2042325.

References

1. Gourc J-P, Camp S, Viswanadham B, Rajesh S. Deformation behavior of clay cap barriers of hazardous waste containment systems: Full-scale and centrifuge tests. *Geotext geomembr*. 2010;28(3):281–291.
2. Peng M, Zhang L. Breaching parameters of landslide dams. *Landslides*. 2012;9:13–31.
3. Sridharan A, Jayadeva M. Double layer theory and compressibility of clays. *Geotechnique*. 1982;32(2):133–144.
4. Tang C, Shi B, Liu C, Zhao L, Wang B. Influencing factors of geometrical structure of surface shrinkage cracks in clayey soils. *Eng Geol*. 2008;101(3–4):204–217.
5. Omidi G, Thomas J, Brown K. Effect of desiccation cracking on the hydraulic conductivity of a compacted clay liner. *Water Air Soil Pollut*. 1996;89:91–103.
6. Tang C-S, Cui Y-J, Tang A-M, Shi B. Experiment evidence on the temperature dependence of desiccation cracking behavior of clayey soils. *Eng Geol*. 2010;114(3–4):261–266.
7. Uday K, Singh D. Investigation on cracking characteristics of fine-grained soils under varied environmental conditions. *Drying Technol*. 2013;31(11):1255–1266.
8. Nahlawi H, Kodikara JK. Laboratory experiments on desiccation cracking of thin soil layers. *Geotech Geol Eng*. 2006;24(6):1641–1664.
9. Griffith A. The theory of rupture. In: *First Int. Cong. Appl. Mech*. 1924:55–63.
10. Konrad J-M, Ayad R. Desiccation of a sensitive clay: field experimental observations. *Can Geotech J*. 1997;34(6):929–942.
11. Hallett P, Newson T. A simple fracture mechanics approach for assessing ductile crack growth in soil. *Soil Sci Am J*. 2001;65(4):1083–1088.
12. Hallett P, Dexter A, Seville J. The application of fracture mechanics to crack propagation in dry soil. *Eur J Soil Sci*. 1995;46(4):591–599.
13. Tang C-S, Zhu C, Cheng Q, Zeng H, Xu J-J, Tian B-G, Shi B. Desiccation cracking of soils: A review of investigation approaches, underlying mechanisms, and influencing factors. *Earth-Sci Rev*. 2021;216:103586. http://dx.doi.org/10.1016/j.earscirev.2021.103586.
14. Zhou L, Zhu Z, Qiu H, Zhang X, Lang L. Study of the effect of loading rates on crack propagation velocity and rock fracture toughness using cracked tunnel specimens. *Int J Rock Mech Min Sci*. 2018;112:25–34. http://dx.doi.org/10.1016/j.ijrmms.2018.10.011.
15. Hatibu N, Hettiaratchi D. The transition from ductile flow to brittle failure in unsaturated soils. *J Agric Eng Res*. 1993;54(4):319–328.
16. Hallett PD. *Fracture Mechanics of Soil and Agglomerated Solids in Relation to Microstructure* (Ph.D. thesis). University of Birmingham; 1996.
17. Hallett P, Newson T. Describing soil crack formation using elastic–plastic fracture mechanics. *Eur J Soil Sci*. 2005;56(1):31–38.
18. Adams M, Williams D, Williams J. The use of linear elastic fracture mechanics for particulate solids. *J Mater Sci*. 1989;24:1772–1776.
19. Veveakis E, Regenauer-Lieb K, Weinberg R. Ductile compaction of partially molten rocks: the effect of non-linear viscous rheology on instability and segregation. *Geophys J Int*. 2014;200(1):519–523.
20. Veveakis E, Regenauer-Lieb K. Cnoidal waves in solids. *J Mech Phys Solids*. 2015;78:231–248. http://dx.doi.org/10.1016/j.jmps.2015.02.010.
21. Chu T, Ranson W, Sutton MA. Applications of digital-image-correlation techniques to experimental mechanics. *Exp Mech*. 1985;25:232–244.
22. Fleureau J-M, Wei X, Ighil-Ameur L, Hattab M, Bicalho KV. Experimental study of the cracking mechanisms of clay during drying. In: *From Fundamentals to Applications in Geotechnics*. IOS Press; 2015:2101–2108.
23. Kézdi Á, Réthàti L. *Handbook of Soil Mechanics, Vol. 1*. Elsevier Amsterdam; 1974.
24. Drucker DC, Prager W. Soil mechanics and plastic analysis or limit design. *Q Appl Math*. 1952;10(2):157–165.
25. Hickman R, Gutierrez M. Formulation of a three-dimensional rate-dependent constitutive model for chalk and porous rocks. *Int J Numer Anal Methods Geomech*. 2007;31(4):583–605.
26. Das BM. *Soil Mechanics : Laboratory Manual*. Oxford University Press; 2013.
27. Chen R, Lindqwister W, Hueckel T, Veveakis M. An experimental study on silt desiccation cracking with different basal constraints and various humidity. In: Pasternak E, Dyskin A, eds. *Multiscale Processes of Instability, Deformation and Fracturing in Geomaterials*. Cham: Springer Nature Switzerland; 2023:144–154.
28. Blaber J, Adair B. Ncorr: open-source 2D digital image correlation matlab software. *Exp Mech*. 2015;55(6):1105–1122.
29. Baker S, Matthews I. Lucas-kanade 20 years on: A unifying framework. *Int J Comput Vis*. 2004;56:221–255.
30. Rattez H, Shi Y, Sac-Morane A, Klaeyle T, Mielniczuk B, Veveakis M. Effect of grain size distribution on the shear band thickness evolution in sand. *Géotechnique*. 2022;72(4):350–363. http://dx.doi.org/10.1680/jgeot.20.P.120.
31. Péron H, Hueckel T, Laloui L, Hu L. Fundamentals of desiccation cracking of fine-grained soils: Experimental characterization and mechanisms identification. *Can Geotech J*. 2009;46:1177–1201. http://dx.doi.org/10.1139/T09-054.
32. Veveakis M, Poulet T. A note on the instability and pattern formation of shrinkage cracks in viscoplastic soils. *Geomech Energy Environ*. 2021;25:100198. http://dx.doi.org/10.1016/j.gete.2020.100198.
33. Peron H, Laloui L, Hueckel T, Hu LB. Desiccation cracking of soils. *Eur J Environ Civ Eng*. 2009;13(7–8):869–888.
34. Chandrasekhar S. *Hydrodynamic and Hydromagnetic Stability*. Dover Publications Inc.; 1961.
35. Costa S, Kodikara J, Barbour S, Fredlund D. Theoretical analysis of desiccation crack spacing of a thin, long soil layer. *Acta Geotech*. 2018;13:39–49.
36. Bourne N, Millett J, Rosenberg Z, Murray N. On the shock induced failure of brittle solids. *J Mech Phys Solids*. 1998;46(10):1887–1908.

37. Mouritz AP. 18 - Fracture processes of aerospace materials. In: *Introduction to Aerospace Materials*. Woodhead Publishing; 2012:428–453. http://dx.doi.org/10.1533/9780857095152.428.
38. Moreland DW. Chapter 17 - mechanical systems safety. In: Musgrave GE, Larsen ASM, Sgobba T, eds. *Safety Design for Space Systems*. Burlington: Butterworth-Heinemann; 2009:549–606. http://dx.doi.org/10.1016/B978-0-7506-8580-1.00017-8.
39. Liu M, Gan Y, Hanaor DA, Liu B, Chen C. An improved semi-analytical solution for stress at round-tip notches. *Eng Fract Mech*. 2015;149:134–143. http://dx.doi.org/10.1016/j.engfracmech.2015.10.004.
40. Oka F, Kimoto S, Higo Y, Ohta H, Sanagawa T, Kodaka T. An elasto-viscoplastic model for diatomaceous mudstone and numerical simulation of compaction bands. *Int J Numer Anal Methods Geomech*. 2011;35(2):244–263.
41. Hacker BR, Christie JM. Brittle/ductile and plastic/cataclastic transitions in experimentally deformed and metamorphosed amphibolite. *Brittle-Duct Transit Rocks*. 1990;56:127–147.
42. Cassiani G, Brovelli A, Hueckel T. A strain-rate-dependent modified Cam-Clay model for the simulation of soil/rock compaction. *Geomech Energy Environ*. 2017;11:42–51. http://dx.doi.org/10.1016/j.gete.2017.07.001.
43. Chen K, Schweizer KS. Theory of yielding, strain softening, and steady plastic flow in polymer glasses under constant strain rate deformation. *Macromolecules*. 2011;44(10):3988–4000. http://dx.doi.org/10.1021/ma200436w, arXiv:https://doi.org/10.1021/ma200436w.
44. Taheri A, Sasaki Y, Tatsuoka F, Watanabe K. Strength and deformation characteristics of cement-mixed gravelly soil in multiple-step triaxial compression. *Soils Found*. 2012;52(1):126–145. http://dx.doi.org/10.1016/j.sandf.2012.01.015.
45. Horseman S, Handin J. Triaxial-compression tests on rocksalt at temperatures from 50° to 200° c and strain rates from 10- 4 to 10- 9/s. *Brittle-Duct Transit Rocks*. 1990;56:103–110.
46. Alevizos S, Poulet T, Sari M, Lesueur M, Regenauer-Lieb K, Veveakis M. A framework for fracture network formation in overpressurised impermeable shale: Deformability versus diagenesis. *Rock Mech Rock Eng*. 2017;50(3):689–703. http://dx.doi.org/10.1007/s00603-016-0996-y.
47. Chen R, Lindqwister W, Wu F, Mielniczuk B, Hueckel T, Veveakis M. The physics of desiccation cracks 2: Modeling and prediction of the crack patterns. *Geomech. Energy Environ.*. 2023. http://dx.doi.org/10.1016/j.gete.2023.100489.